

# Computational fluid dynamics modelling of flow and energy fluxes for a natural fluvial dead zone

## Modélisation en dynamique des fluides numérique des transferts de débit et d'énergie dans une zone morte fluviale naturelle

B.G. HANKIN\*, M.J. HOLLAND, K.J. BEVEN AND P. CARLING<sup>+</sup>, IENS, Lancaster University, \* now at the Scottish Environment Protection Agency, Castle Business Park, Stirling, FK9 4TR, <sup>+</sup> now at the Southampton University, UK.

### ABSTRACT

This study links together information that characterizes the energy and momentum fluxes across the shear zone between the main flow and a dead zone in the UK on the River Severn [1-3]. The depth-averaged flow in and around the dead zone is modelled using TELEMAC-2D, with semi-distributed eddy viscosity and bed roughness, and compares well with some distributed field measurements within the reach. The resulting velocity field is then used to provide momentum fluxes for a finite difference model incorporating finite volumes (FDFV model) numerical scheme that has been developed to solve depth averaged advection-diffusion of thermal energy in a body fitted co-ordinate system. Assuming that buoyancy forces can be neglected, the gross hydraulics of the system explains much of the temperature distribution that was observed using infra-red aerial imagery.

### RÉSUMÉ

Cette étude relie les informations qui caractérisent les flux d'énergie à ceux de quantité de mouvement, à travers la zone de cisaillement située entre l'écoulement principal et une zone morte de la rivière Severn au Royaume-Uni. L'écoulement moyenné en hauteur dans la zone morte et à l'extérieur de celle-ci est calculé par TELEMAC-2D, avec une viscosité turbulente et une rugosité du fond semi-distribuées ; il se compare bien aux champs de mesures disponibles. Le champ de vitesse calculé est alors utilisé pour fournir les flux de quantité de mouvement à un modèle numérique en différences finies - volumes finis (modèle FDFV) qui résout l'équation de transport-diffusion de l'énergie thermique dans un système de coordonnées curvilignes. En supposant que les effets de densité sont négligeables, l'hydraulique globale du système explique bien la répartition de température qui avait été observée par imagerie infra-rouge aérienne.

Key words: dead zone, finite volume, energy fluxes, remote sensing.

### 1 Introduction

Dead zones are slow moving or recirculating regions of water with high residence times compared with the main flow. This fluid retention is important to the longitudinal dispersion characteristics of a complex river flow, giving rise to the long tail in concentration break-through curves [4-7]. The processes governing fluid fluxes across strong transverse shear layers affect both solute and suspended sediment dynamics [1], and the resilience of some ecological systems. The impetus for the present study stems from the efficiency gains that could be made in large scale river studies, if remotely sensed thermal images such as in figure 1 could be used to glean spatial information about the hydraulics which has in part generated the observed temperature distribution. Effective flood modelling and water quality modelling are also dependent on a good understanding of this type of cross-shear interaction [8]. Studies of the turbulent fluxes of mass and momentum across transverse shear layers within an engineered flume flow [9-12] has resulted in a better understanding of the effect that the shear has on the overall dynamics and the resulting dispersion characteristics of the flow. Fluxes across a region of shear between a dead zone and main flow have been modelled using computational fluid dynamics by [13, 14], guided by understanding of the same recirculation process generated by groynes [15], strong secondary circulation [16] or overbank flow [17]. In this study the St Venant equations for shallow water are closed

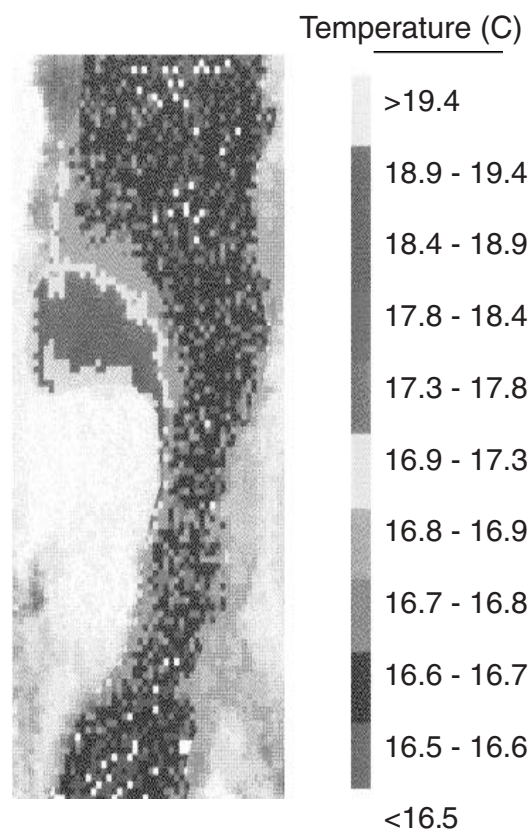


Fig. 1. NERC Daedalus AADS thermal line scanner image of study reach containing large dead zone, after Reynolds et al., 1991 [36]

Revision received April 20, 2001. Open for discussion till December 31, 2002.

using a simple semi-distributed eddy viscosity scheme, whereby the eddy viscosity is varied discretely between different zones within the reach. There are many numerical schemes that are more sophisticated than this, including ones that solve higher order non-linear eddy viscosity closures, or Reynolds stress models which solve the equations of transport of turbulent momentum fluxes (for example, see [18]). For this study, the relatively simple model was utilised since it retains sufficient flexibility to capture the observed functionality of the system, but makes few claims to represent the precise turbulent behaviour of the flow. Indeed, there are a host of models and model structures which would achieve this, giving rise to the phenomenon of equifinality ([8, 10, 11, 19-21]) in models for complex systems. The non-linearity of the governing flow equations means that every scale of motion from the dissipative, to the gross swirling motions can be mutually dependent, and are affected by the complex geometry of the river boundary conditions. It is useful to consider the relative merit of different models [8] which capture the correct functionality of the system, as far as we are able to assess it on the basis of what are usually limited field measurements.

## 2 Monitoring

The study site on the River Severn at Leighton, near Shrewsbury, UK, is characterized by a large, stable bar, downstream of which there exists a pool of slow moving or recirculating water, apparent from the warmer surface water on the left side of figure 1. The figure relates to the surface water alone, since the outgoing radiation is emitted primarily from a very thin layer at the top of the water column.

However, further measurements of temperature throughout the water column indicate that between 2pm and 8pm, on a warm summer day, the water is well mixed and that the remotely sensed image (taken at approximately 3pm) gives a good indication of the local depth averaged temperature for these conditions. Therefore, the warmer patches of water were considered to have been generated in regions of shallow water, where there is significant mixing and less volume of water to heat up. During the heating up period of the diurnal cycle, the water surface temperature in the dead zone was observed to heat up more slowly than the water in the rest of the water column. Over this period, the temperature difference between the water surface and the depth-averaged temperature was of the order of 1 to 2 degrees Celsius.

The detailed flow measurements were conducted for a single low flow of approximately 12.8 cumecs, although it is considered that

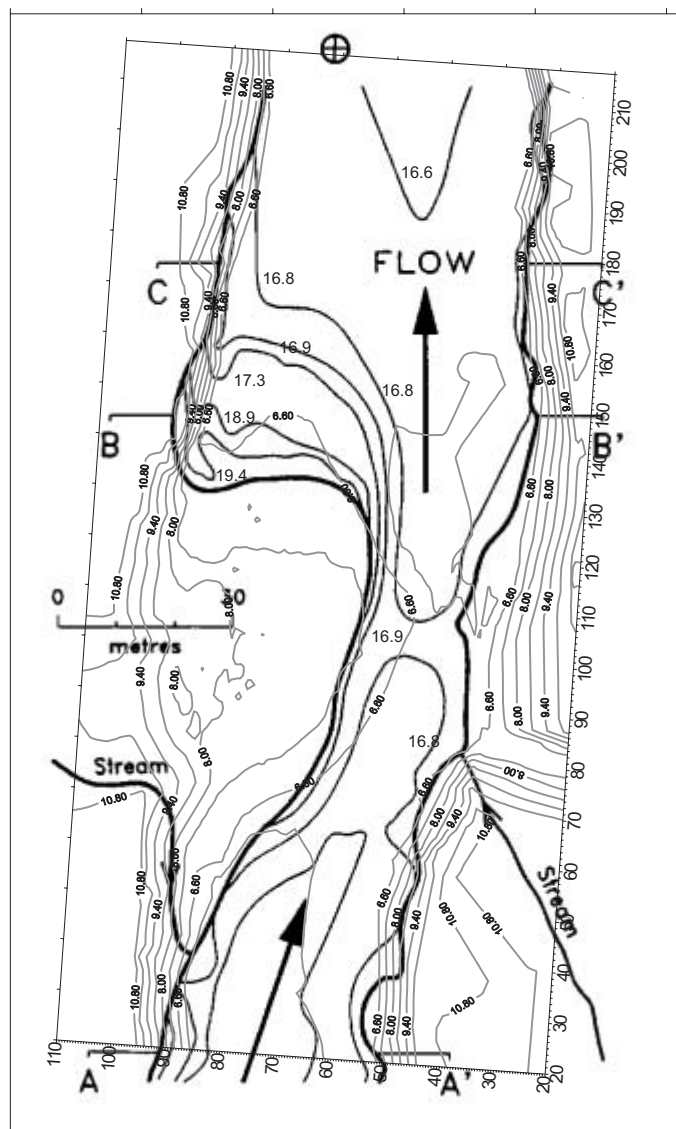


Fig. 2. Overlay of remotely sensed temperature distribution onto the river bed topography

the observed recirculation will be representative of most low to medium flows, where there is no significant over-bar flow. This is supported by [22] where it is reported that the volumetric effect of the dead zone on the dispersion process is only weakly dependent on the discharge. The details of the surveyed bathymetry are given in figure 2, along with a superposition of the temperature distribution shown in figure 1. The topography used in the modelling process is given in figure 3, where the bank sides are approx-

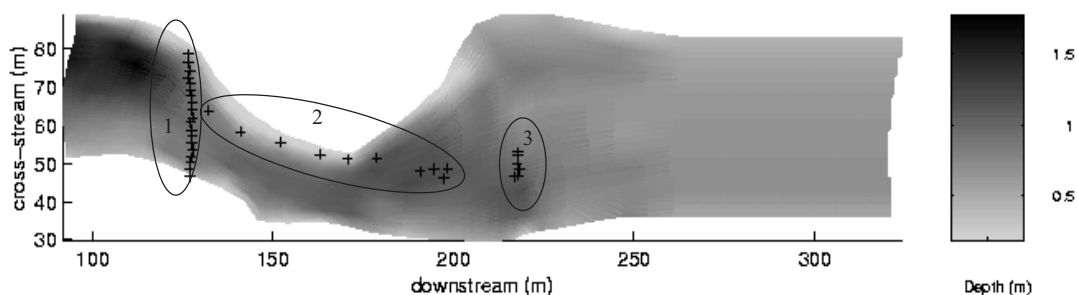


Fig. 3. Contour plot of the topography used by the flow models, with velocity measurement sites shown

imated as being vertical. The sites at which detailed flow measurements were made are indicated in figure 3. At these sites up to 6 measurements of the local flow velocities were made through the depth using an array of electromagnetic current meters (ECMs). These measurements through the depth were then depth averaged for each site and the local downstream depth averaged velocity components could then be compared with the model predictions at each site.

### 3 Primary modelling process

#### 3.1 Approximations and assumptions

TELEMAC2D solves numerical approximations to the depth averaged, Reynolds averaged, Navier-Stokes equations for fluid flow [23]. The model is accurate only for approximately hydrostatic situations, where there are negligible vertical accelerations, and has been developed for the case with negligible mean vertical velocities, which is an adequate assumption for the flow studied here. This above restriction also indicates that secondary circulation (with a downstream component of vorticity) cannot be modelled explicitly in TELEMAC-2D, but the effect that such differential advections have on the rates of dispersion is modelled by assuming that this component of the secondary circulation can be incorporated by using an enhanced diffusion coefficient. It also assumes that the surface and bed are impermeable and that the bed material is static.

The set of flow equations were closed using a semi-distributed eddy viscosity, or parameter relating the local turbulent momentum fluxes and the mean velocity gradients. This procedure is an approximate mechanism by which to model the bulk diffusion of momentum down a momentum gradient. The eddy viscosity was given different values in different zones within the reach to reflect the inhomogeneous nature of turbulent momentum transfer. Three distinct zones were defined, each taking different values of eddy viscosity, these being the main stream, the dead zone, and the shear zone separating the two. Anisotropy in the turbulence field is also responsible for generating turbulent induced secondary advections[24], but because some components of vorticity cannot be modelled, whatever additional vorticity is generated by these anisotropies in the real system, must be accounted for using an additional component to the eddy viscosity.

A TELEMAC-2D algorithm was used to estimate the inlet transverse velocity profile. This uses a parabolic relationship with em-

pirical shape parameters, and the maximum velocity is adjusted such that the integral of the depth averaged velocity over the cross section is equal to the measured discharge (Environment Agency data). The algorithm also makes the assumption that the water surface slope is parallel to the bed slope at this point, 100m upstream of the true inlet cross section. The first 100m of the flow domain was included as a run-in section to allow for the parabolic profile to develop into a more realistic velocity profile across the inlet. It is acknowledged that flows profiles are rarely parabolic, and that the run-in section is relatively short. However, the profile was observed to develop away from a parabola into a shape that was approximately consistent with the profile that was measured some distance downstream (see Section 3.3 and figure 5). In addition to the inlet flow specification, the stage was fixed at the downstream outlet, allowing the model to specify both the velocities and distributed free surface elsewhere, but still giving a well posed numerical problem.

The values of turbulent eddy viscosity used for the three zones described above were selected following a sensitivity analysis and are given in Table 1. The dimensions and vigorousness of the recirculation were sensitive to variations in these three parameters, although there were also multiple model structures which yielded similar patterns, giving rise to the problem of equifinality [8]. The viscosities indicate the relative strength of transverse turbulent mixing, and are generally considered to scale with the local transverse component of Reynolds stresses (which can be interpreted as turbulent fluxes of momentum). The ratio of the zonal viscosities to each other (Table 1, column 5), is similar to the measurements of Reynolds stress components taken using an Acoustic Doppler Velocimeter (ADV) for another relatively low flow.

#### 3.2 Bed and side wall friction

The Mannings roughness coefficient, was allowed to take on values in the three zones between  $0.01 \text{ m}^{-1/3}\text{s}$  and  $0.05 \text{ m}^{-1/3}\text{s}$ . Chow [25] relates a value of Mannings n of  $0.05 \text{ m}^{-1/3}\text{s}$  to a stony stream and so relatively large values for a lowland river were investigated since these coefficients control the momentum and energy losses incurred for a depth averaged flow. It is known a priori that they are often required to be artificially high, in order to model the effective losses due to 3 dimensional turbulent effects. For instance, the vertical upwelling (burst) of water from the bed with slow downstream velocity which retards the flow nearer to the

Table 1 Parameterisation of TELEMAC-2D

Quantity/Zone	Main flow	Shear zone	Dead zone	Ratio
Measured transverse Reynolds stress component 0.4m above bed, and co-ordinate of measurement representative of zone	$0.479 \text{ kgm}^{-1}\text{s}^{-2}$ (x=98.81,y=42.628)	$2.053 \text{ kgm}^{-1}\text{s}^{-2}$ (x=45.829, y=113.012)	$0.09\text{kgm}^{-1}\text{s}^{-2}$ (x=56.384, y=158.44)	1 : 4.3 : 0.2
Eddy viscosity used in Telemac2D	$0.01 \text{ m}^2\text{s}^{-1}$	$0.5 \text{ m}^2\text{s}^{-1}$	$0.001 \text{ m}^2\text{s}^{-1}$	1 : 10 : 0.1
Mannings n used in TELEMAC-2D	$0.015 \text{ m}^{-1/3}\text{s}$	$0.05 \text{ m}^{-1/3}\text{s}$	$0.05 \text{ m}^{-1/3}\text{s}$	

free surface, cannot be modelled explicitly in the depth averaged case, but its effect is lumped into an effective roughness.

Side-wall friction was incorporated in TELEMAC-2D using a simple constraint on the normal derivative of the depth-averaged velocity component that is parallel to the local wall boundary, which is used as  $\kappa$ - $\epsilon$  equation boundary conditions [23] in TELEMAC-2D. The constraint imposes an exponential retardation of velocity between the node adjacent to the boundary and the boundary, with an exponent argument given by equation 1:

$$a = -\frac{u_*^2}{U_{ig} v_T} \quad (1)$$

Using a reach-averaged estimate of the shear velocity ( $u_*$ ) of  $0.046 \text{ ms}^{-1}$ , (estimated from field measurements of the velocity profiles in the main channel and dead zone by [1]), reach averaged boundary-adjacent node velocity ( $U_{ig}$ ) of  $0.1 \text{ ms}^{-1}$ ; and the reach averaged value of eddy viscosity ( $v_T$ ) of  $0.008 \text{ m}^2\text{s}^{-1}$ , this gives a value of the coefficient  $a$  value of approximately -1. The coefficient controls the rate of decrease of the velocity between the boundary-adjacent node and the boundary.

### 3.3 The discretisation scheme

Figures 4(a-d) indicate the flow and water surface elevation patterns obtained using two meshes, comprising 3500 and 6300 nodes (7000-12000 elements). The elements were made using a constant size criteria, to avoid preconceptions of where regions of strong solution variable gradients might be, and to allow for fairer inter-comparison of the performance of different resolutions.

Good flow predictions in terms of the fit to the available data were found for the two different meshes that were investigated, as indicated by figures 5a and 5b, with coefficients of determination of 0.44 and 0.48 for the coarse and fine resolution figures respectively (see section 4). The predictions made using the fine resolution mesh were then interpolated onto the coarse resolution mesh using an inverse distance method. The closeness of fit between the two sets of predictions gave a coefficient of determination of 0.87, which indicates an acceptable degree of grid independence for this kind of complex domain. It has been noted by several authors (for example, see [26]), that for different resolution meshes applied to complex geometry river topographies, not only does the topographic representation change, but the values of roughness parameters must also be changed in order to consis-

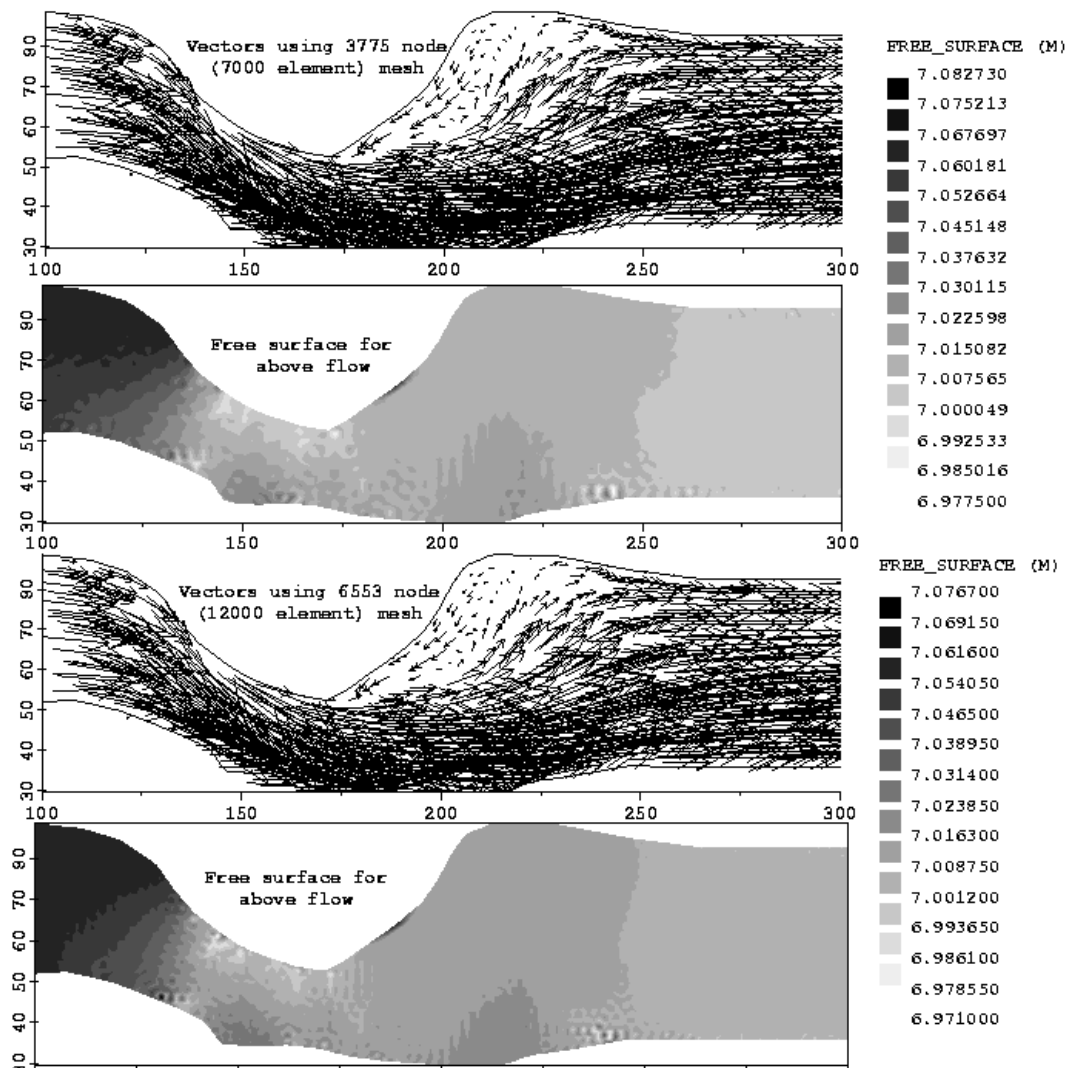


Fig. 4. Mesh used by TELEMAC-2D, contour map of predicted water surface elevation and velocity vectors

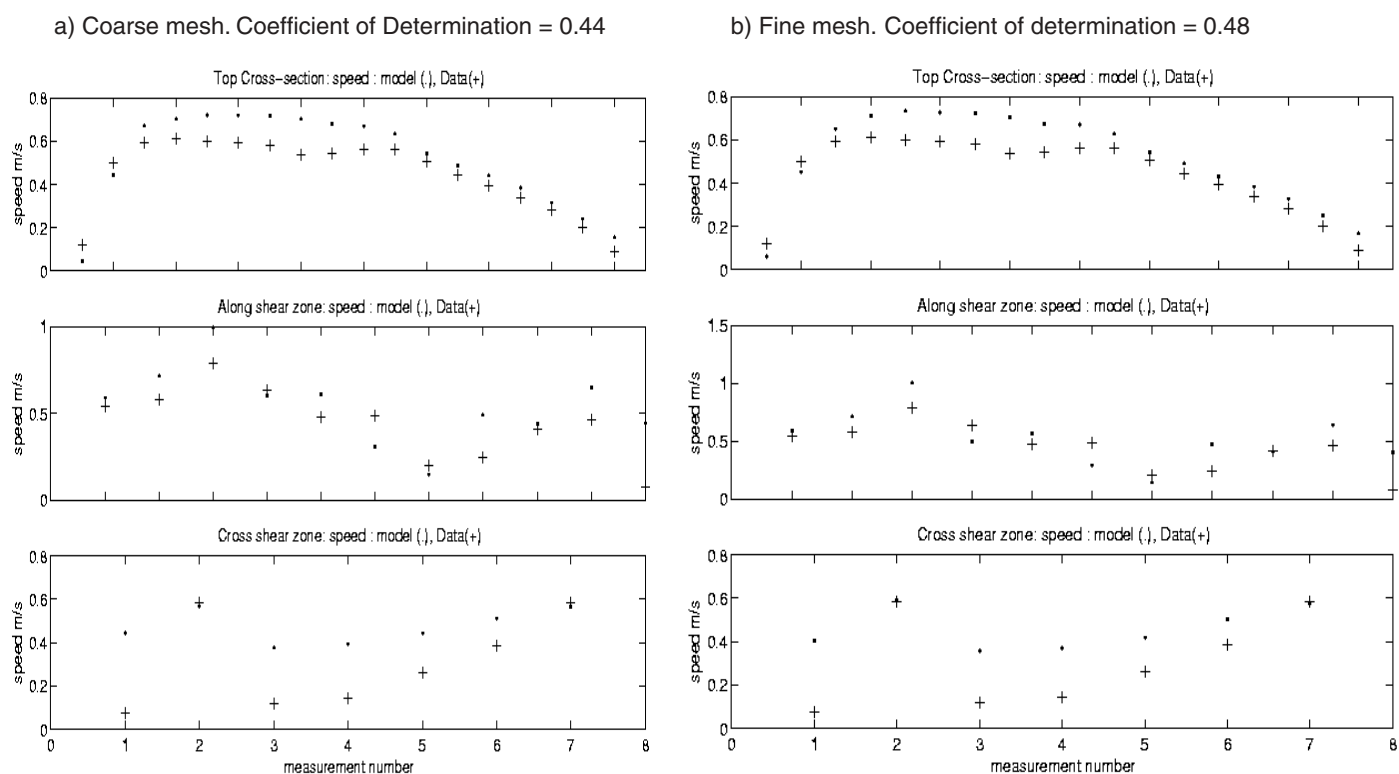


Fig. 5. Comparison of predicted and measured velocities at the sites marked in figure 3

tently predict distributed measurements (such as point measurements of velocities). This is hardly surprising, given that the roughnesses which are used in a depth averaged model are ‘effective’ parameters, which control the *grid scale* rates of energy and momentum losses, but which represent an integration of the effect that sub-grid processes are having on the flow as a whole. For the comparison that was made in this study none of the boundary conditions were varied between the meshes. The finer resolution mesh was used for the remainder of the study, although either mesh could have been utilised.

The conservative streamline upwind Petrov-Galerkin (SUPG) numerical scheme was used to model the advection of depth in the continuity equation, forcing conservation of mass everywhere except at the downstream boundary, where the free surface was imposed. An implicit ‘N’ scheme which is unconditionally stable was used for the advective velocities.

A one second time step was used, in order to maintain a Courant number of approximately unity, and the model was run for 10,000 and 20,000 time steps. The two simulations using a 3500 node mesh yielded a whole field residual (between the above successive computations) of  $0.0009 \text{ ms}^{-1}$  and  $0.002 \text{ ms}^{-1}$  for downstream (U) and cross-stream (V) velocities respectively. The slight difference may reflect inaccuracies in the numerical scheme, or the unsteadiness in the solution due to vortices generated downstream of the bar. The two solutions at 10,000 and 20,000 time steps yielded measures of fit to the depth averaged flow data that were within less than 0.3% of each other.

#### 4 Results of application of primary modelling process

Figures 4b and 4d indicates that there is a steady water surface drop of a few centimeters over the reach of interest. The velocity vector plot in figures 4a and 4c are for the best fitting model structure, with distributed Manning and eddy viscosity coefficients given in Table 1. The vectors indicate that the zone of recirculation is restricted to about 20 m downstream of the flow separation point, which is consistent with field observations for low flows. The relative possibility that different model structures provided good simulations of the system was assessed on the basis of a measure of closeness of fit between the predicted velocities and the depth averaged velocity data, at the sites indicated in figure 1. This measure was the coefficient of determination,  $O_1$ , given by equation 2:

$$O_1 = 1 - \frac{\epsilon^2}{\sigma_{data}^2} \quad (2)$$

$$\epsilon^2 = \sum_{i=1}^{N_m} (v_i^{prediction} - v_i^{data})^2 / N_m$$

where  $\epsilon^2$  is the mean of the squared residuals,  $v^{prediction}$  and  $v^{data}$  are the predicted and calculated depth averaged velocities at site  $i$ , and  $N_m$  is the total number of measurements sites, which was 35.

Figures 5a and 5b show the closeness of fit to the depth averaged data, which have been divided into regions 1-3, indicated in figure 3, those of the top cross section, along the shear (approximately superimposed along the observed shear zone) and the cross shear section. It can be seen that the cross shear zone (where there are large transverse gradients of velocity) is most

difficult to fit but that the overall best fitting model gave an overall closeness of fit to the data with a coefficient of determination of 0.48. This was considered to be a sufficiently good simulator of the system to move on to the secondary modelling process, in which the energy budgets are considered.

### 5 The secondary modelling process

The velocities predicted from the primary modelling process were now used to drive a depth averaged, FDFV model of the advection and diffusion of heat, which was based upon a similar body fitted co-ordinate system to the model of Rodi et al. [27]. A coarse grid was constructed for speed of operation, and the distributed fluxes as predicted by TELEMAC2D were calculated in the TELEMAC-2D post-processing package RUBENS (developed at LNH, Electricité De France) across the faces of the finite volume grid indicated in figure 6. The determination of distributed fluxes in this way from a finite element solution is problematic owing to the possible local non-conservative nature of the finite element technique. The SUPG scheme is globally mass conservative, although the distributed fluxes are not guaranteed to be at a local scale, especially if linear bases functions are used for interpolating both depth and velocity to determine fluxes.

The FDFV grid comprised 28 columns of 9 cells in the cross stream direction, forming 29 cross sections. The mean and standard deviation from the mean of the vector flux across each cross-section was determined to be 12.82 +/- 0.06 cumecs using RU-

BENS, the latter indicating that the errors in mass conservation are small (< 0.5%). The non-conservativeness may have arisen from a number of sources, such as the approximations due to the use of linear bases functions in the version of TELEMAC-2D that was used, the bi-linear interpolation scheme of RUBENS, or possibly due to unsteadiness in the flow solution, although this was considered to be small (see end of section 3).

To ensure non-divergence of the FDFV scheme, the cells must be corrected to be locally conservative. The correction procedure comprised five steps given in Appendix 1, and resulted in the corrected conservative fluxes shown in figures 6a and figure 6b. The correction algorithm given in Appendix 1 is not necessarily unbiased, and would not be recommended for the correction of strongly non-conservative fields. However, the magnitude and distribution of the changes that were made to the fluxes to achieve conservativeness are shown in figure 6c and 6d, and indicate that the approach is reasonably unbiased for this application, and that the corrections are small.

The Governing equation for the transport of a passive scalar in steady, two dimensional flows in orthogonal co-ordinates given by the advection diffusion equation:

$$\frac{\partial}{\partial x}(U\phi + \Gamma \frac{\partial \phi}{\partial x}) + \frac{\partial}{\partial y}(V\phi + \Gamma \frac{\partial \phi}{\partial y}) = 0 \quad (3)$$

where  $\phi$  is a passive scalar, and will represent temperature in rela-

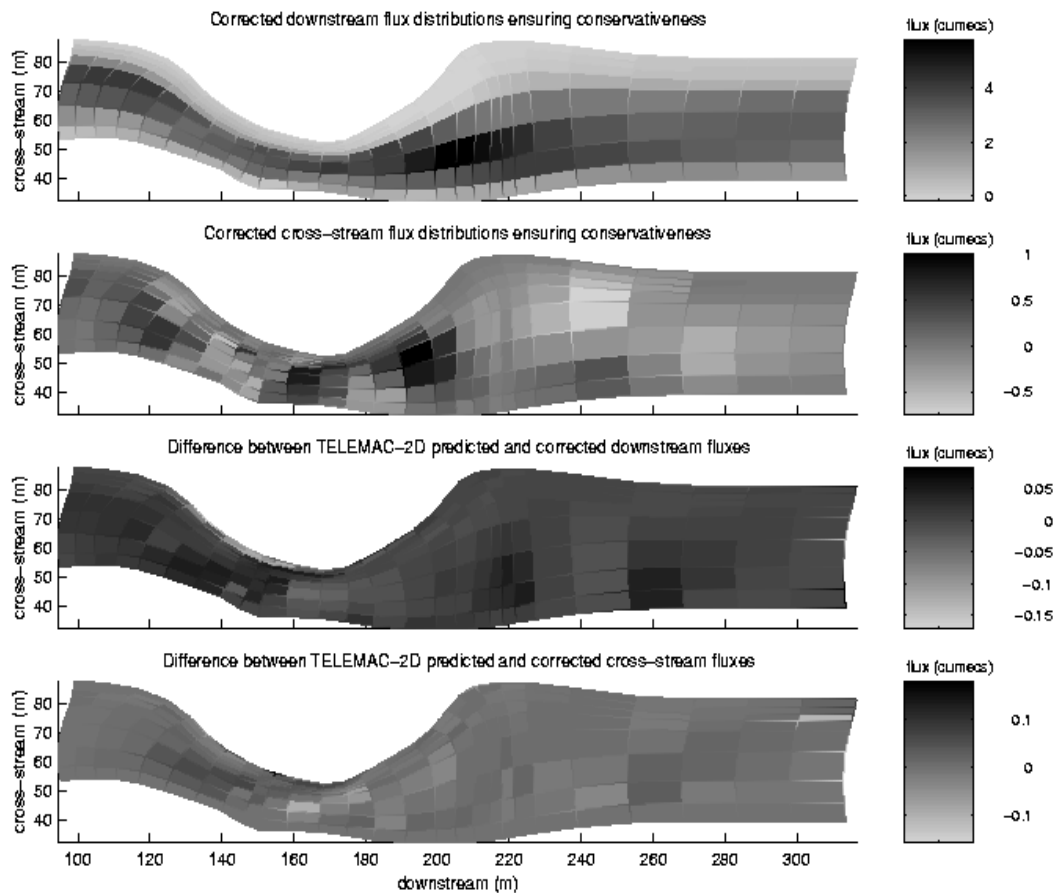


Fig. 6. Contour map of FDFV model fluxes c

tion to this study, and x and y are the orthogonal axes, with  $\Gamma$  a local diffusivity. For non-orthogonal co-ordinates, this must be transposed into the local co-ordinate system (axes  $x_1$  and  $x_2$  in figure 7), as given in Rodi et al. [27], which need not be reproduced here because the application of the FDFV technique results in a simple balance between the advective and diffusive fluxes across the common faces of each control volume (the solid trapezium in figure 7). The discretised equation is simply an expression of the balance between these different fluxes, and is hence locally and globally mass conservative.

The local fluxes across each face are calculated using the product of the local components of velocity (from the TELEMAC-2D simulation) and geometrical factors indicated as  $b^1_{1e}$ , etc, which ensure that the correct component of the fluxes are used. The fluxes are evaluated at each face, in a way that is consistent between control volumes. The expression for the convective and diffusive fluxes of  $\varphi$  through the cell face e, for example are given by equations 4 and 5 respectively, after Rodi et al. [27]:

$$I_e^C = \rho r_e (b_1^1 v_1 + b_2^1 v_2)_e \varphi_e = U_e \varphi_e \quad (4)$$

$$I_e^D = I_e^{DN} + I_e^{DC} = - \left( \frac{\Gamma_\varphi}{\Delta V} \right)_e D_{1e}^1 (\varphi_E - \varphi_P) - \left( \frac{\Gamma_\varphi}{\Delta V} \right)_e D_{2e}^1 (\varphi_{ne} - \varphi_{se}) \quad (5)$$

where

$$D_{1e}^1 = r_e^2 (b_1^1 b_1^1 + b_2^1 b_2^1) \quad D_{2e}^2 = r_e^2 (b_1^2 b_1^2 + b_2^2 b_2^2) \\ D_{1e}^2 = D_{2e}^1 = r^2 (b_1^2 b_1^1 + b_2^2 b_2^1)$$

where  $\Delta V$  is a control cell volume, and where each  $\Delta V_e$  (for east face) term is calculated from the shaded area centered on the cell face, e in figure 7.  $r_e$  is the local depth at the centre of a control volume face,  $\rho$  is water density, and  $I_e^C$  represents the convective mass flux across face e, and the 'b' and 'D' terms are geometrical

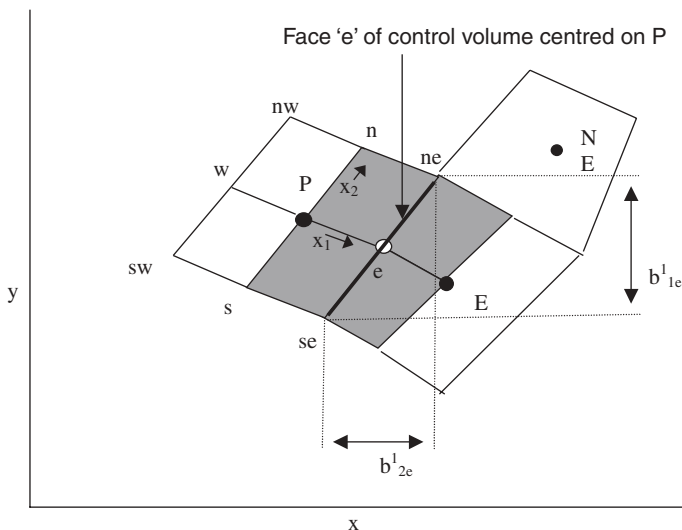


Fig. 7. Control volume diagram

factors for the determination of the correct component of flux normal to the cell faces.

Estimation of the value of  $\varphi_e$  for the convective term, was formulated implicitly using the hybrid difference scheme in terms of the adjacent control volume, central node values ( $\varphi_P, \varphi_N$ , etc in figure 7) given by equation 6:

$$\varphi_e = \varphi_P C_A^e + \varphi_E C_B^e \quad \text{for } |P_e| \geq 2 \\ \varphi_e = \text{interpolation between } \varphi_P \text{ and } \varphi_E \quad \text{for } |P_e| < 2 \quad (6)$$

where

$$C_A^e = [0.5(U_e + |U_e|)/U_e] \quad C_B^e = [0.5(U_e - |U_e|)/U_e]$$

and with the magnitude of the Peclet number given by  $|P_e| = U_e (\Delta V)_e / (\Gamma_e D^1)_e$ , where  $\Gamma_e$  is the local diffusivity. The value of the solution variable at the cell face e ( $\varphi_e$  for example) was determined simply through inverse distance weighting of the values of the solution variable at nodes P and E. The values of  $\varphi$  at the cell faces that were required in the evaluation of the normal diffusive flux,  $I^{DN}$  and the cross-diffusive flux,  $I^{DC}$  (both of these were determined using second order accurate, central differences) were also linearly interpolated with distance between adjacent cell nodes.

The two diffusive fluxes,  $I^{DN}$  and  $I^{DC}$ , coupled with the convective flux,  $I^C$ , are next expressed by equation (7) as a balance between advection and diffusion in 2 dimensions, for all unbounded cells:

$$U_{2n} (C_A^n \varphi_P + C_B^n \varphi_N) - U_{2s} (C_A^s \varphi_S + C_B^s \varphi_P) + \\ U_{1e} (C_A^e \varphi_P + C_B^e \varphi_E) - U_{1w} (C_A^w \varphi_W + C_B^w \varphi_P) = \\ \Gamma_{nV} D_{2n}^2 (\varphi_N - \varphi_P) - \Gamma_{sV} D_{2s}^2 (\varphi_P - \varphi_S) + \\ \Gamma_{eV} D_{1e}^1 (\varphi_E - \varphi_P) - \Gamma_{wV} D_{1w}^1 (\varphi_P - \varphi_P) + \\ \Gamma_{nV} D_{2n}^1 (\varphi_W - \varphi_E) / 2 - \Gamma_{sV} D_{2s}^1 (\varphi_W - \varphi_E) / 2 + \\ \Gamma_{eV} D_{2e}^1 (\varphi_N - \varphi_S) / 2 - \Gamma_{wV} D_{2w}^1 (\varphi_N - \varphi_S) / 2 + \\ \Gamma_{eV} D_{2e}^1 (\varphi_{ne} - \varphi_{se}) - \Gamma_{wV} D_{2w}^1 (\varphi_{nw} - \varphi_{sw}) + \\ \Gamma_{nV} D_{1n}^2 (\varphi_{ne} - \varphi_{nw}) - \Gamma_{sV} D_{1s}^2 (\varphi_{se} - \varphi_{sw}) \quad (7)$$

where for instance  $\Gamma_{eV}$  is the local diffusivity divided by the local value of  $\Delta V_e$ .

In this scheme the corner values of the solution variable, such as  $\varphi_{ne}$ , in the cross-diffusive terms (see [27], [28]) on the 4<sup>th</sup> line are determined from the closest 4 adjacent node values (N, NE, E and P for  $\varphi_{ne}$ , for example see [29] and [30].) instead of incorporating them as source terms as in [26], and by using an inverse distance weighting for each term of the form given by equation 8:

$$\varphi_{ne} = \frac{\varphi_N w_N^{ne} + \varphi_{NE} w_{NE}^{ne} + \varphi_E w_E^{ne} + \varphi_P w_P^{ne}}{den^{ne}} \quad (8)$$

where

$$den^{ne} = w_N^{ne} + w_{NE}^{ne} + w_E^{ne} + w_P^{ne}$$

$$w_n^{ne} = 1 / |ne - NE|$$

where  $|ne-NE|$  is the distance between points ne and NE in figure 7. Similar expressions are determined for the value of  $\phi$  at each of the other corner nodes. Having formulated expressions for the different fluxes, the complete set of discrete equations were expressed in the generic form of equation (9) after [31]:

$$a_p \phi_p = a_w \phi_w + a_e \phi_e + a_s \phi_s + a_n \phi_n + S_U \quad (9)$$

where upon re-arranging, the 'a' coefficients are given by:

$$a_p = [U_{2n} C_A^n - U_{2s} C_B^s + \Gamma_{nV} D_{2n}^2 + \Gamma_{sV} D_{2s}^s + U_{1e} C_A^e - U_{1w} C_B^w + \Gamma_{eV} D_{1e}^1 + \Gamma_{wV} D_{1w}^1] - a_p^{DC}$$

where

$$a_p^{DC} = \left[ \left( \frac{W_p^{ne}}{den^{ne}} - \frac{W_p^{se}}{den^{se}} \right) \Gamma_{eV} D_{2e}^1 - \left( \frac{W_p^{nw}}{den^{nw}} - \frac{W_p^{sw}}{den^{sw}} \right) \Gamma_{wV} D_{2w}^1 \right. \\ \left. + \left( \frac{W_p^{ne}}{den^{ne}} - \frac{W_p^{nw}}{den^{nw}} \right) \Gamma_{nV} D_{1n}^2 - \left( \frac{W_p^{se}}{den^{se}} - \frac{W_p^{sw}}{den^{sw}} \right) \Gamma_{sV} D_{1s}^2 \right]$$

$$a_w = [U_{1w} C_A^w + \Gamma_{wV} D_{1w}^1 + \Gamma_{nV} D_{2n}^1 / 2 - \Gamma_{sV} D_{2s}^1 / 2] + a_w^{DC}$$

$$a_s = [U_{2s} C_A^s + \Gamma_{sV} D_{2w}^2 - \Gamma_{eV} D_{2e}^1 / 2 + \Gamma_{wV} D_{2w}^1 / 2] + a_s^{DC}$$

$$a_n = [-U_{2n} C_B^n + \Gamma_{nV} D_{2n}^2 + \Gamma_{eV} D_{2e}^1 / 2 - \Gamma_{wV} D_{2w}^1 / 2] + a_n^{DC}$$

$$a_e = [-U_{1e} C_B^e + \Gamma_{eV} D_{1e}^1 - \Gamma_{nV} D_{2n}^1 / 2 - \Gamma_{sV} D_{2s}^1 / 2] + a_e^{DC}$$

where the cross diffusive components at the end of each of the lower 4 expressions are similar to  $a_p^{DC}$ . The source term  $S_U$  is zero for the unbounded cases, unless heat is explicitly added to the cell. For boundary-adjacent nodes  $S_U$  becomes non-zero, and if, for example,  $\phi$  is equal to  $\phi_A$  at a western boundary, then all of the terms involving  $\phi_w$  are substituted for  $\phi_A$ , and become absorbed into the source term,  $S_U$  as in [30]. This also modifies the coefficient  $a_p$ , which must have the term  $-S_U/\phi_A$  added in the set of linear equations generated from equation 9 above.

A simple single-direction sweeping scheme was then used for a series of steady flow calculations. This involved solving the flux balance equations in a cross-stream direction, with upstream water temperatures fixed at known values ( $\phi_w, \phi_{SW}$  and  $\phi_{NW}$ ), left and right bank temperatures fixed, but with downstream temperatures guessed ( $\phi_e, \phi_{SE}$  and  $\phi_{NE}$ ). The fixed bank temperature is not corroborated by data other than the remotely sensed data, but the approach assumes that under the water, the bank remains slow to respond to diurnal changes in ground surface or water surface warming, and instead remains at the ambient temperature of the water (16.6C).

The resulting set of linear equations were solved using the in-built MATLAB Gaussian elimination scheme, and this provided the set of cells just downstream with new upstream boundary conditions. The process was repeated until the final set of cross-stream cells was reached, where the downstream boundary condition was assumed to be zero temperature gradient. The values of temperature of all the cell centres were then stored. The whole sweeping process was repeated, and the new distributed temperatures were again stored. The whole-field average (over every centre-cell esti-

mation of temperature for the entire reach) of the squared differences between the temperatures of these successive sweeps was then determined, and the sweeping process was iterated until this whole-field mean residual reduced to a very small amount.

A further test for the flow model conservativeness was included by setting the diffusivity to zero, and checking for convergence of this scheme. For the case of zero source term, the numerical scheme rapidly converged, with a drop of the mean of the whole field residual value from unity to 0.0008 over 20 sweeps.

### 5.1 Thermal budget model assumptions

It is postulated that the most important mechanisms for heat transport within the flow are the gross advective and diffusive fluxes due to the flow alone, and that if net energy source or sink terms and boundary conditions for temperature distribution are known for a certain flow, then the model described above ought to be sufficient to predict steady state temperature distributions. The temperature diffusivity coefficient was set equal to the semi-distributed eddy viscosity (viscosity rather than kinematic viscosity) in the three different zones, since we are implicating that the only significant diffusion arises from the turbulent momentum fluxes, and that in this case the Reynolds Analogy can be used.

The most important sources of heating come from the three components of net radiative transfer due to insolation and exchanges of sensible and latent heat fluxes with the lower atmosphere, for which measurements were made within and around the dead zone in mid July and are given in figure 8. Evans et al. [32] found that the total energy gains in the flow were dominated by net short-wave radiation contributing on average 97.6% of the total energy gain, similar to this study (see figure 8). Webb and Zhang [33] also found that inputs of energy into a river were dominated by radiative fluxes, with net radiation receipt accounting for on average around 90% of the non-advective total in both summer and winter.

Evans et al. [32] found that on average 82 % of the total energy transfers occurred at the air-water interface for a shallow river (0.18m), but that 15% of the total energy exchanges occurred at the channel bed, owing to a difference in temperature between the hyporeic zone and the overlying water. Webb and Zhang [33] found different results for different rivers, but for the river Bere, which had some weed cover, conductive losses were reduced to less than 1% in the summer months. This agrees with findings on the River Severn, in which the total energy losses were dominated by the radiation from the water surface, and conductive losses through the bed were minimal. This was supported by the measured water temperature profile within the dead zone (figure 9), which was found to show very little or no vertical temperature gradient near to the bed. Also evident from figure 9, the temperature at all depths was influenced strongly by the summertime diurnal cycle. Groundwater heat fluxes, and heat changes due to internal friction were deemed to be negligible (for example, see [34]).

The temperature of the banks was assumed to warm up and cool down more rapidly than the river water, assuming a lower specific heat capacity, such that for the half hourly time steps used

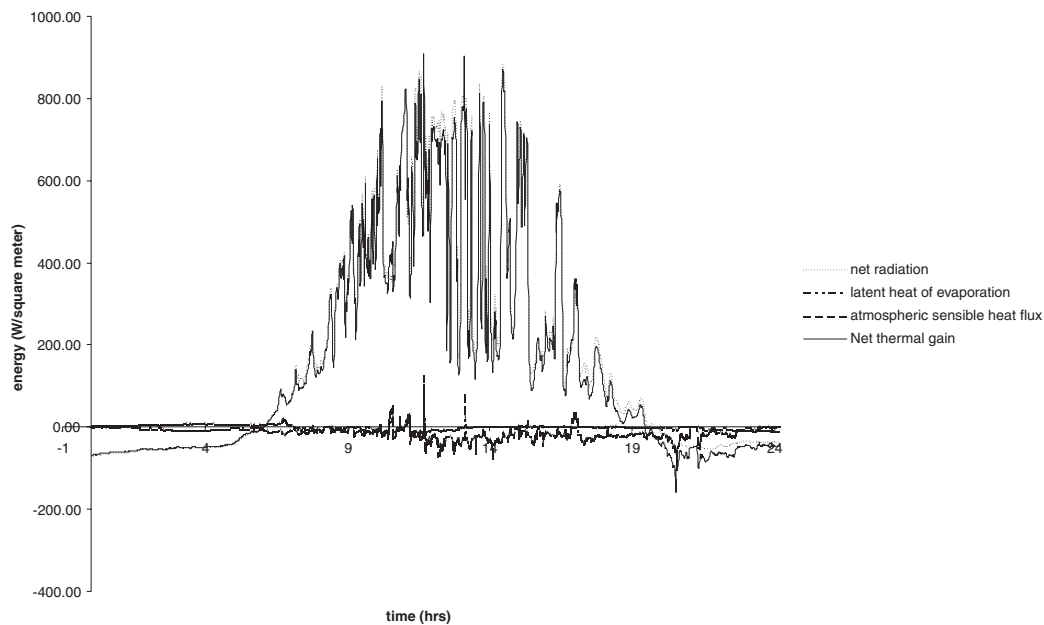


Fig. 8. Energy flux budgets into and out from the dead zone

in the energy budget model, the ambient net radiative heat flux dictated the bank temperature. It was assumed that a viscous sub-layer of immobile water was in constant thermal contact with the bank.

### 5.2 Diurnal temperature prediction

Having made these assumptions about the different fluxes and boundary conditions, the FDFV model was used to predict the temperature distribution in the river as a series of steady states (using half hourly steps over 24 hours). The mean temperature of the water at the outlet to the reach was also used as a cyclic boundary condition and re-applied to the inlet at the start of each

new time step. This therefore incorporated the heating that the water upstream of the study reach had received during the previous time step. A completely unsteady solver was avoided in order to simplify the modelling procedure, and it was considered that the use of a series of steady states was sufficient, given the large time scales of the dynamics involved.

It was also assumed that the net energy absorbed at the water surface becomes rapidly well mixed, and results in a net temperature change over the entire water column of each cell, for each half hour time step, which is largely justified by 13 out of 15 of the thermocouples warming up in synchrony in figure 9, arriving at the first peak approximately in phase around 2 pm, and remaining approximately equal. The trace of the uppermost thermocouple in

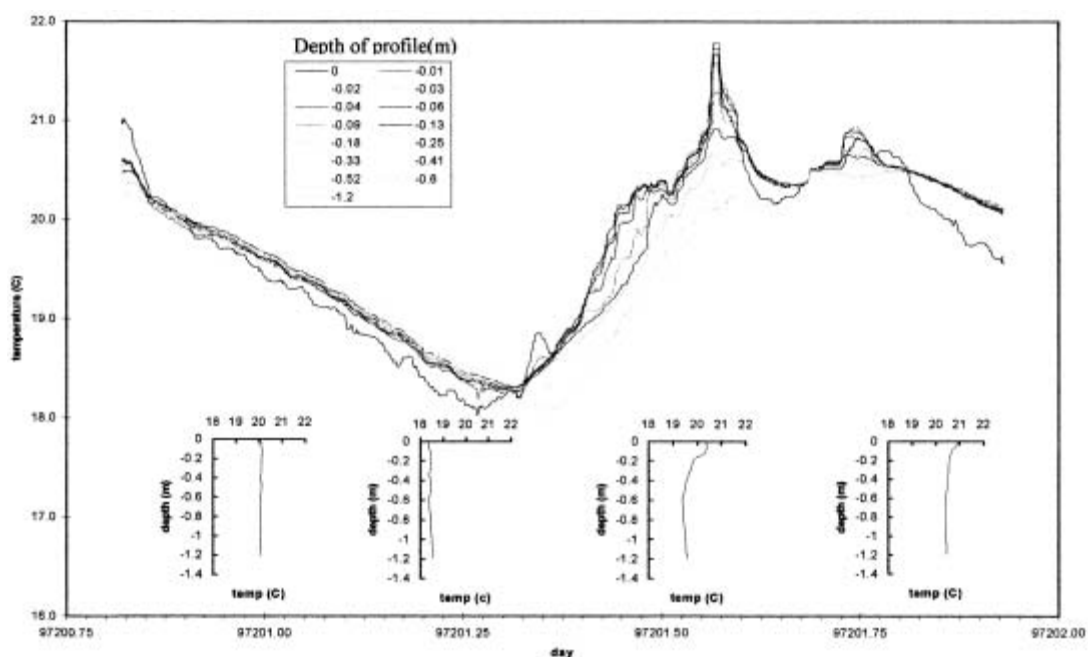


Fig. 9. Depth-wise temperature variations in the dead zone

figure 9 should be treated with caution, since it was half in of the water and half in the air, and could have been too strongly influenced by the ambient air temperature. Figure 10 shows the relation of the temperature in the uppermost 1 mm of the water column, in relation to the depth averaged temperature. The two traces are close in value for most of the day, apart from a discrepancy of 1-1.5 degrees during the warming up part of the cycle. Figure 11 shows the set of steady states obtained using the time averaged net heat flux (from figure 8) as a source for each control volume, and by making the above approximation that the net radiative forcing rapidly affects the whole of the water column. The sub-plots within figure 11 indicate that the dead zone takes some time to warm up, but that around 3 pm (the time of day that the remotely sensed image was taken), the depth averaged temperature distribution is qualitatively very similar to the remotely sensed image, of figure 1, taken a few years previously. The flow and radiation conditions may have differed between the two sets of data, although both the over-flight and velocity measurements were taken on warm, clear skied summer days. The difference between the traces in figure 10 was used to correct the predicted depth averaged temperatures in order to estimate the water surface temperature over the warming up period. A coefficient of determination (using equation 2, substituting the predicted and observed velocities for predicted and observed water surface temperatures) was then calculated for the goodness of fit between the observed and corrected water surface temperature. The best fit occurred around 4-5 pm, with a coefficient of deter-

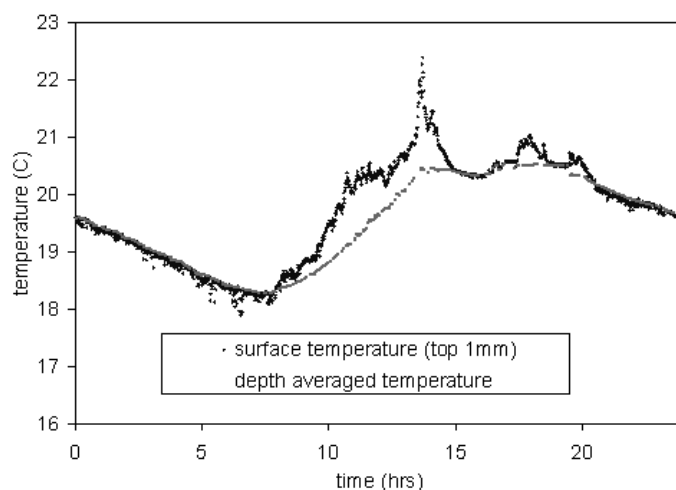


Fig. 10. Relationship between depth averaged temperature and surface layer temperature

mination of 0.29. This quantitative comparison should be treated with caution, and results of a further over-flight for the dates on which the velocity and energy budget measurements were taken are awaited before drawing any strong conclusions. There are a number of refinements that would clearly need to be made in order to transport the model to other rivers, and for it to take into account seasonality, scale effects and flow regime. Inclusion of other sources or sinks of energy, such as bed conduction is simple to implement with the FDFV scheme.

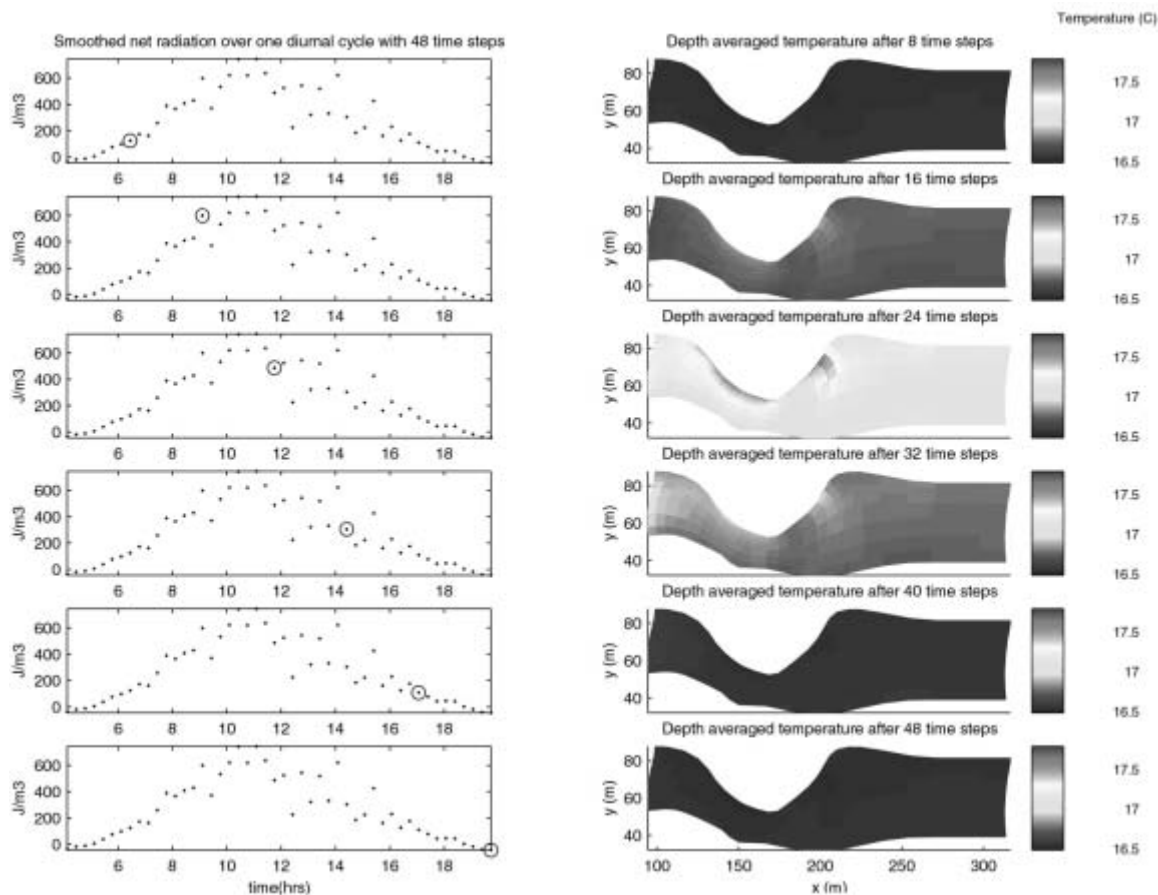


Fig. 11. Set of steady state temperature distributions under diurnal net radiation forcing

## 6 Conclusions

A depth averaged numerical approximation to the St. Venant equations for shallow water flow was used to model the flow around a dead zone feature on a reach of the River Severn. The semi-distributed eddy viscosity and roughness coefficient were varied until there was a relatively good fit between the predicted depth averaged velocities and the depth average of the measured velocities. The predicted velocity field was then used to supply a finite difference based on finite volume (FDFV) model implementation of the 2D advection diffusion equation. It is possible to model the gross energy budgets across a large region of shear using a relatively simple, mass conservative FDFV approach. The conservativeness property of the FDFV scheme makes the solution of the advection diffusion equation highly transparent, and lends itself well to the incorporation of other source / sink terms that are often specified component-wise in river energy budget studies. It has been established that the gross hydraulics appear to explain the pattern of temperature distribution within the river reach, and consequently, simple inspection of a remotely sensed image such as figure 1, may lead to greater efficiency in the estimation of how river flows are behaving. Since this paper was written some first attempts have been made to do this using an adaptive neural network fuzzy inference system [35].

## Appendix A

The algorithm that was used to ensure local conservativeness is given in the following 5 steps which result in the small corrections given in figures 6c and 6c.

Step 1: The downstream flux ( $I^e$  or  $I^w$ ) for each column (cross section) of cells was normalised to the mean (12.82 cumecs) in order to conserve the total flux across any transect:

$$I_{correction1}^e = I_{Telemac}^e \cdot \frac{12.82}{\sum_j I_{Telemac}^e} \quad (A1)$$

where the suffix *correction1* indicates the corrected flux after the first step of correcting the fluxes from the finite element model (suffix *Telemac*). The process was carried out for every column of cells shown in figure 6, and amounted to a correction of less than 0.5% for any cell. Each column of cells is thus forced to be conservative (there are no fluxes from the banks).

Step 2: The net flux for every cell in the FDFV grid, starting at the furthest upstream cell closest to the right bank (cell  $i=1, j=1$ ) was determined. For local conservativeness, the net flux must equal zero for every cell. For each cell  $i, j$ , the residual flux,  $R_{i,j}$ , was determined as:

$$R_{i,j} = I_{i,j}^e + I_{i,j}^w + I_{i,j}^n + I_{i,j}^s \quad (A2)$$

where for example  $I^e$  is the total flux across face e, and R is the

residual flux (typically of the order 0.001 to 0.01 cumecs). Starting with cell  $i=1, j=1$ , there is no flux from the right bank ( $I^s = 0$ ), so only  $I^n, I^e$  and  $I^w$  can be corrected in order to make the net flux equal zero. This is achieved through subtracting  $R/3$  from the flux across each face.

Step 3: The previous step results in the total downstream flux for column 1 no longer equating to 12.82, by an amount equal to  $R/3$  for each face (e and w), so in step 3 the downstream fluxes ( $I^w, I^e$ ) for each of the remaining cells ( $i=2$  to 8) for column 1 are increased by an amount  $R/(3 \times 8)$  (then by factors  $R/(3 \times 7)$ ,  $R/(3 \times 6)$ , etc for cells  $i=3, 4$ , etc). This maintains both the conservativeness of the column of cells, and the conservativeness of the individual cell that has just been corrected.

Step 4: Steps 2 to 3 are repeated for cells 2 to 8, noting that the excess flux R for each cell is still only divided between  $I^e, I^w$  and  $I^n$  for all cells,  $I^s$  having been fixed as the correction process progresses from s to n. Since the conservativeness of column of cells 1 to 9 has been maintained at each step, and since after this step cells 1 to 8 have been forced to be conservative, cell 9 is forced to be locally conservative, and no further correction is required.

Step 5: The next column of cells is corrected in the same way as for steps 1 to 5 above, except the flux across the upstream faces ( $I^w$ ) is not allowed to change – the residual flux R has to be divided between  $I^n$  and  $I^e$  only for step 2. The process is repeated for all of the columns until every cell is locally conservative. Since some of the cells occupy regions where the flow across a particular face is low, a further constraint was included which weighted the corrections so that faces with the largest fluxes received the greater proportion of the residual, R, in steps 2 and 3, hence minimising the percentage changes imposed.

The correction algorithm is not necessarily un-biased, and would not be recommended for the correction of strongly non-conservative fields. However, the magnitude and distribution of the changes that were made to the fluxes to achieve conservativeness are shown in figure 6c and 6d, and indicate that the approach is reasonably unbiased for this application, and that the corrections are small.

## List of symbols

$a$	coefficient determining side-wall friction
$\phi$	passive scalar – also representative of temperature here
$\phi_p$	value of passive scalar at centre of cell labelled P
$N, S, E, W$	nodes adjacent to node labelled P, using compass bearings for direction
$n, s, e, w$	faces of control volume with centre node labelled P, also using compass bearings for direction.
$ne, nw, sw, se$	corners of control volume with centre node labelled P, also using compass bearings for direction.
$u_*$	friction velocity
$U_{tg}$	tangential velocity at boundary adjacent node
$\nu_T$	turbulent kinematic eddy viscosity
$\epsilon^2$	mean of the squared residual

$\sigma_{\text{data}}^2$	standard deviation from the mean of the observations
$v^{\text{prediction}}$	predicted depth averaged velocity
$v^{\text{data}}$	calculated depth averaged velocity
$N_m$	Total number of measurements sites
$O_1$	Coefficient of determination
$U_1$	Local downstream velocity
$U_2$	Local cross-stream velocity
$r$	flow depth
$\Delta V$	control cell volume
$r$	local depth of the control volume
$I$	Total flux across a face indicated by a suffix
$R$	Residual flux determined from summation of vector fluxes across all faces of a cell
$I_e^C$	convective flux across face e
$\rho$	density of water
$b_2^1$ , etc.	geometric correction factors for evaluation of fluxes
$v_1, v_2$	local components of velocities at control volume faces
$U_1, U_2$	velocity vector at cell face
$I^D$	combined diffusive flux across cell face
$I^{DN}$	normal diffusive flux
$I^{DC}$	cross diffusive flux arising due to non-orthogonality of local co-ordinates
$\Gamma$	diffusivity coefficient
$D_1^\varphi$ , etc.	geometric correction term for local flux balance

## Acknowledgements

This work has been supported by NERC grants GR3/10687 and GR3/09742. The authors wish to express their gratitude to: the two referees for their helpful comments; J.M. Hervouet for the use of the TELEMAC-2D code; J.Freer for support in using the LINUX PC cluster; John Baugh for TELEMAC-2D support; R.Oakey for help in collecting field data. We also owe a debt of gratitude professor Stuart Lane, Dr Richard Hardy and Dr Helen Kettle, whose comments improved the paper.

## References

- Carling, P.A., H.G. Orr, and M.S. Glaister, *Preliminary observations and significance of dead zone flow structure for solute and fine particle dynamics*, in *Mixing and Transport in the environment*, K.J. Beven, P.C. Chatwin, and J.H. Millbank, Editors. 1994.
- Heslop, S.E., M.J. Holland, and C.A. Allen, *Turbulence measurements in the River Severn*, in *Mixing and Transport in the environment*, K.J. Beven, Chatwin, P.C., and Millbank, J.H., Editors. 1994, Wiley.
- Tipping, E., C. Woof, and K. Clarke, *Deposition and resuspension of fine particles in a riverine deadzone*. Hydrological Processes, 1989. 7: pp. 263-277.
- Wallis, S.G., Young, P.C. and Beven, K.J., *Experimental investigation of the aggregated deadzone model for longitudinal solute transport in stream channels*. Proc. Inst. Civ. Engin., 1989. 87(2): pp. 1-22.
- Heslop, S.E. and C.M. Allen, *Modelling dispersion in the River Severn using a random walk model*. Journal of hydraulics research, 1993. 31(3): pp. 323-331.
- Young, P.C. and S.G. Wallis, *Solute transport and dispersion in channels*, in Channel Network Hydrology, K.J. Beven and M. Kirkby, Editors. 1993, Wiley.
- Rutherford, J.C., *River mixing*. 1994: Wiley.
- Hankin, B.G., Hardy, R. Kettle, H. and Beven, K.J., *Using CFD in a GLUE framework to model the flow and dispersion characteristics of a natural fluvial dead zone*. Earth Surface Processes and Landforms, 2001. 26, pp 667-687.
- Knight, D.W. and K. Shiono, *Turbulence measurements in a compound overbank flow*. Journal of hydraulic research, 1989. 28(2).
- Hankin, B.G. and K.J. Beven, *Modelling dispersion in complex open channel flows: (1) Equifinality of model structure*. Stochastic Hydrology and Hydraulics, 1998a. 12(6): pp. 377-396.
- Hankin, B.G. and K.J. Beven, *Modelling dispersion in complex open channel flows: (2) Fuzzy calibration*. Stochastic Hydrology and Hydraulics, 1998b. 12(6): pp. 397-412.
- Guymet, I., *Longitudinal Dispersion in sinuous channels with changes in shape*. Journal of hydraulic engrg., 1998. 35.
- Kimura, I. and T. Hosoda, *Fundamental properties of flows in open channels with dead zone*. Journal of Hydraulic Engineering, 1997. Feb.: p. 98.
- El Latif, M.A., Campbell, C.W. *Effect of deadzones on natural stream transport*. in *Int. Conference On Water Res. Engineering*. 1995.
- Ouillon, S. and D. Dartus, *Three dimensional computation of flow around groyne*. Jn. of hydr. research, 1997: pp. 962.
- Hodskinson, A., *Computational fluid dynamics as a tool for investigating seperated flow in river bends*. Earth surface processes and landforms, 1996. 21: pp. 993-1000.
- Knight, D.W. and K. Shiono, *River channel and Floodplain hydraulics*, in *Floodplain Processes*, M. Anderson, Walling, D.E. and Bates, P.D., Editor. 1996, Wiley.
- Younis, B.A., *Progress in turbulent modelling for open-channel flows*, in *Flood plain Processes*, M.G. Anderson, D.E. Walling and P.D. Bates, Editors. 1996, Wiley & Sons.
- Beven, K.J., *Prophecy, reality and uncertainty in distributed hydrological modelling*. Advances in Water Research, 1993. 16: pp. 41-51.
- Beven, K.J. and A. Binley, *The future of distributed models: model calibration and uncertainty prediction*. Hydrological Processes, 1992. 6: pp. 279-298.
- Aronica, G., Hankin, B.G. and K.J. Beven, *Uncertainty and equifinality in calibrating distributed roughness coefficients in a flood propagation model with limited data*. Advances in Water Resources, 1998a. 22(4): pp. 349-365.
- Beven, K.J. and P.A. Carling, *Velocities, roughness and dispersion in a lowland River Severn*, in *Lowland Floodplain Rivers: Geomorphological Perspectives*, P.A. Carling and G.E. Petts, Editors. 1992, Wiley: Chichester. p. 71-93.

23. Hervouet, J.M. and L. Van Haren, *TELEMAC-2D Version 3.0 Principal note*, . 1995, EDF-DER, France.
24. Cokljat, D. and B.A. Younis, *Compound channel flows - a parametric study using a Reynolds stress transport closure*. Journal of Hydraulics Engineering, ASCE, 1995. 33(3): pp. 307-320.
25. Chow, V.T., *Open Channel Hydraulics*. 1959: McGraw-Hill Book Co.
26. Hardy, R.J., P.D. Bates, and M.G. Anderson, *The importance of spatial resolution in hydraulic models for floodplain environments*. Journal of Hydrology, 1999. 216: pp. 124-136.
27. Rodi, W., S. Majumdar, and B. Schonung, *Finite volume methods for two-dimensional incompressible flows with complex boundaries*. Computer methods in applied mechanics and engg., 1989. 75: pp. 369-392.
28. Demirdzic, I., Gosman, A.D., Issa, R.I. and Peric, M., *A calculation procedure for turbulent flow in complex geometries*. Computers and fluids, 1987. 15(3): pp. 251-273.
29. Maliska, C.R. and G.D. Raithby, *A method for computing three dimensional flows using non-orthogonal boundary-fitted co-ordinates*. Int. Jn. For Num. Meth. In Fluids, 1984. 4: pp. 519-537.
30. Zhou, J.G. and I.M. Goodwill, *A finite volume method for steady state 2D shallow water flows*. International Journal of Numerical Methods for Heat Loss and Fluid Flow, 1997. 7(1): p. 4-23.
31. Versteeg, H.K. and W. Malalasekera, *Computational fluid dynamics: the finite volume method*. 1995: Longman.
32. Evans, E.C., McGregor, G.R., Petts, G.E., *River energy budgets with special reference to river bed processes*. Hydrological Processes, 1998. 12: pp. 575-595.
33. Webb, B.W. and Y. Zhang, *Water Temperatures and heat budgets in Dorset chalk water courses*. Hydrological Processes, 1999. 13: p. 309-321.
34. Joss, J. and G. Resele, *Mathematical modelling of the heat exchange between a river and the atmosphere*. Boundary layer meteorology, 1987. 41: pp. 27-40.
35. Hankin, B.G. Kettle. H, Beven, K.J., *Fuzzy Mapping of momentum fluxes in complex shear flows with limited data*, Journal of Hydroinformatics, 2001, (03.2) pp 91-103.
36. Reynolds, C.S., Carling, P.A., Beven, K.J. *Flow in river channels: new insights into hydraulic retention*. Archiv. Hydrobiol. 1991, 121, pp 171-179.